

Elastocapillarity at Cell-Matrix ContactsXuechen Shi,¹ Zezhou Liu,² Luyi Feng,³ Tiankai Zhao,³ Chung-Yuen Hui,² and Sulin Zhang^{1,3,4,*}¹*Department of Biomedical Engineering, Pennsylvania State University,
University Park, Pennsylvania 16802, USA*²*Department of Mechanical and Aerospace Engineering, Field of Theoretical and Applied Mechanics,
Cornell University, Ithaca, New York 14853, USA*³*Department of Engineering Science and Mechanics, Pennsylvania State University,
University Park, Pennsylvania 16802, USA*⁴*Department of Material Science and Engineering, Pennsylvania State University,
University Park, Pennsylvania 16802, USA* (Received 20 October 2021; revised 31 January 2022; accepted 4 April 2022; published 7 June 2022)

At cell-matrix contacts, an elastocapillary effect arises in addition to active cell traction. The coexistence of active extracellular traction and other interfacial forces at the contacts blurs their distinctive roles in tissue morphogenesis, wound healing, and cancer metastasis. Here, we first observe that cell colonies can indent soft hydrogels, forming dimples. At inhibited cell contractility, the dimples still occur but with a reduced depth. To exclude active cell traction at the cell-matrix contact, we inhibit cell contractility and measure the interfacial stresses at the colony-hydrogel-medium three-phase interfaces using the Neumann triangle method. The critical elastocapillary length scale of the colony-hydrogel contacts is found to be comparable to the cell colony size, at which the classical Johnson-Kendall-Roberts contact theory fails. Theoretical and computational models suitable for different critical elastocapillary length scales are developed to predict the elastocapillarity-induced indentation depth. A two-step traction force microscopy is, therefore, proposed to separate active cell traction from the interfacial stresses. By quantifying the elastocapillary effect separated from active cell traction, our study lays down a foundation for understanding a variety of elastocapillarity-induced mechanobiological processes in cells and tissues.

DOI: [10.1103/PhysRevX.12.021053](https://doi.org/10.1103/PhysRevX.12.021053)Subject Areas: Biological Physics, Mechanics
Soft Matter**I. INTRODUCTION**

Contacts are ubiquitous in living organisms. At the cell-cell and cell-extracellular matrix (ECM) contacts, intercellular adherens junctions and focal adhesions are active interfacial mechanical switches that transmit cellular forces. On the other hand, much like a small droplet on an elastic substrate, capillary force arises at the cell-ECM contacts, wetting the ECM [1–3] and modulating tissue morphogenesis and growth. Examples of interfacial force regulated cellular processes [4,5] range from cell sorting of a heterogeneous cell mixture from different germ layers [6–10], endocytosis of nanoparticles [11–13], cell adhesion and spreading on various ECMs [14,15], wound healing

[16,17], chemotaxis and mechanotaxis [18–20], and cancer metastasis [21,22], etc. Despite its significant role, capillary force at cell-ECM contacts has been often overlooked. The coexistence of active cell traction and capillary force at cell-ECM contacts, if not separated, may blur their distinctive roles in various mechanobiological processes. For example, it remains elusive as to how the capillary force may initiate mechanotransduction and regulate tissue morphogenesis, repair, and metastasis.

While elastic deformation may occur at all the length scales, capillary forces are usually negligible at large scales for solid surfaces. The relative significance of capillary force to the elastic restoring force defines a critical elastocapillary length $l_S = \gamma/G$, where γ is the interfacial stress and G is the shear modulus of the materials in contact. At a length scale $l \gg l_S$, the capillary effect is negligible and elastic restoring force is dominant, while at $l \ll l_S$, the capillary force overpowers the elastic restoring force. For an interface with a stiff solid of GPa modulus, l_S is on the atomic scale, which suggests that the elastocapillarity effect on stiff solids is important only for nanometer-scale structures. For interfaces of highly compliant

*Corresponding author.
suz10@psu.edu

Published by the American Physical Society under the terms of the [Creative Commons Attribution 4.0 International license](https://creativecommons.org/licenses/by/4.0/). Further distribution of this work must maintain attribution to the author(s) and the published article's title, journal citation, and DOI.

materials, such as hydrogels and soft tissues, l_s can be at the micron scale or even larger.

We here quantify and separate the active cell traction and the interfacial force at the cell-ECM contacts. When cell contractility is inhibited, active cell traction at the cell-ECM contact dissolves, and we denote the remaining force acting on the cell-ECM contact as interfacial (capillary) force. We first show that human colon carcinoma (HCT-8) cell colonies can indent into soft polyacrylamide (PAA) and biopolymeric hydrogels in a colony-size-dependent manner. Indentation still occurs but with a reduced depth when cell contractility is inhibited, suggesting both active cell traction and the interfacial force contribute to the indentation. To determine the critical elastocapillary length scale, we measure the interfacial stresses at the colony-medium-hydrogel three-phase interfaces using the Neumann triangle method (NTM) at inhibited cell contractility. Our measurements show that the critical elastocapillary length is on the same level of the cell colony size, suggesting that the elastocapillary effect is essential for such cell-ECM contacts. Our theoretical and computational models further reveal that the classical Johnson-Kendall-Roberts (JKR) [23–26] fails for the colony-hydrogel contracts due to the capillary forces and the large elastic deformation of the cell colonies. Finally, we suggest a two-step traction force microscopy (TFM) to separate the active traction from the interfacial stresses. Our work sets a basis for the study of capillary forces as one of the external mechanical cues that direct cell migration and tissue morphogenesis.

II. RESULTS

A. Indentation of HCT-8 colonies into soft hydrogels

HCT-8 cells are seeded on fibronectin-coated soft PAA hydrogels with a Young's modulus of 0.5 kPa. Within 12 h of seeding, the cells form cohesive colonies with various sizes (Fig. S1 [27]). Confocal microscopy images show that the colonies are indented into the soft hydrogels (Fig. 1), forming dimples. The dimples remain under inverted culture, suggesting a negligible role of inertia or gravity in dimple formation [Fig. 1(c)]. Upon removal of the cell colonies with sodium hydroxide, the hydrogel surface returns to its flat state (Fig. S2 [27]), indicating that the indentation is fully elastic but not due to plasticity or degradation of the hydrogel. Similar dimples are also observed for a Madin-Darby canine kidney (MDCK) epithelial cell cluster and a single NIH/3T3 mouse fibroblast cell on polyacrylamide hydrogels (Fig. S3 [27]) and for HCT-8 cell colonies cultured on the collagen and fibrin hydrogels (Fig. S4 [27]).

Actomyosin motors empower cell contractility. The contractile forces in the actin stress fibers are transmitted to the substrate through focal adhesion points, generating extracellular traction at cell-ECM contacts. To exclude the effect of active cell traction on dimpling, we add blebbistatin in high concentration (25 μM), which is expected to inhibit more than 90% of cell contractility [22,28,29]. We find that dimples still form in the hydrogels despite a reduced dimple depth [Fig. 1(c)], suggesting that active cell traction contributes to the dimpling but is not a necessary factor.

We next explore the dimple depth for different PAA hydrogel stiffnesses and cell colony sizes at inhibited cell

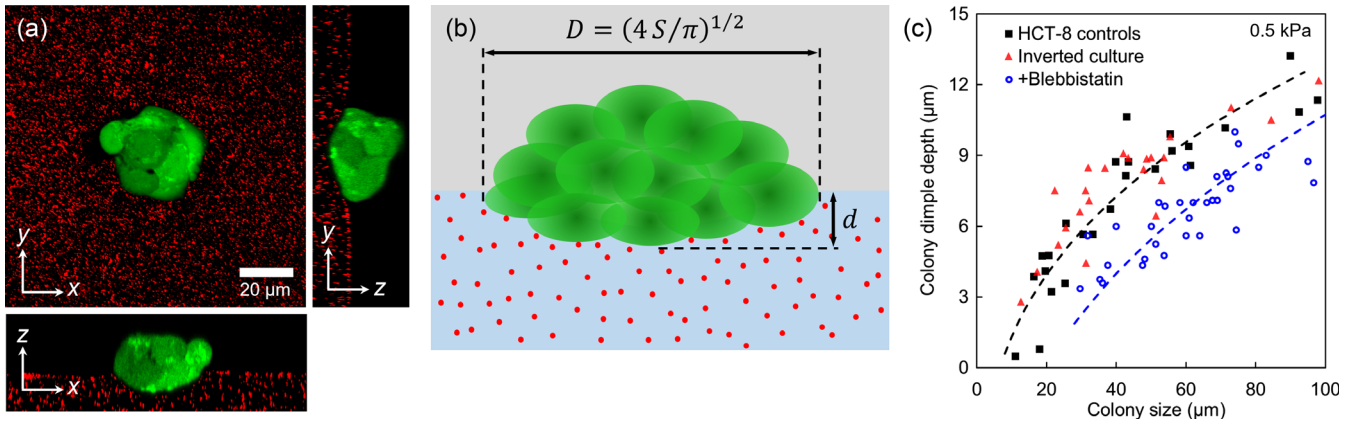


FIG. 1. HCT-8 colony indentation into soft PAA hydrogels. (a) Confocal images of colony indentation into the hydrogel. Cells live-stained with fluorescein diacetate (FDA) show green fluorescence, and the hydrogels are imbedded with red fluorescent beads. (b) Schematic of the configuration for the cell culture system containing an HCT-8 colony, hydrogel, and culture medium. Green: live cells stained with FDA. Light blue: hydrogel substrate embedded with red fluorescent beads. Gray: cell culture medium. Colony size is denoted as the equivalent diameter $D = (4S/\pi)^{1/2}$, where S is the projected colony area. The colony is indented into the soft hydrogels, forming a dimple with depth d . (c) Colony size dependence of cell dimpling into the 0.5 kPa hydrogel. Colony size is denoted as the equivalent diameter calculated by the equation above. Black squares show the dimpling for the control HCT-8 colonies, while red triangles show the dimpling for the inverted cell culture. With blebbistatin, represented by blue circles, the dimples remain but the dimple depths are reduced for all of the colony sizes. Each datum point represents the dimple depth from one colony. Each group contains the combined data from three parallel experiments. The dashed lines are best-fit trend lines of the data points.

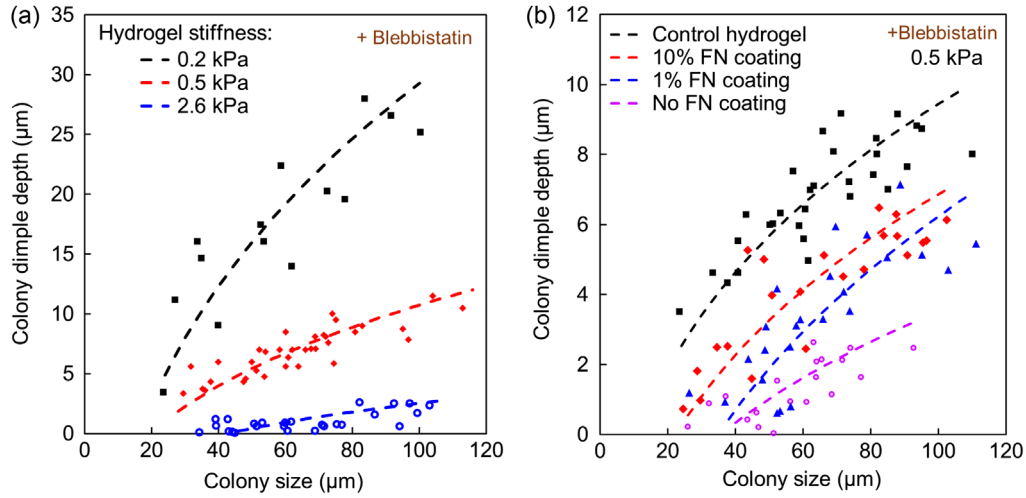


FIG. 2. HCT-8 colony dimpling into PAA gels driven by cell-hydrogel adhesion. (a) Hydrogel stiffness and size-dependent dimpling of the HCT-8 colonies. (b) Effects of fibronectin coating density on HCT-8 colony dimpling. Each group contains the combined data from three parallel experiments. Colony size is denoted as the equivalent diameter $D = (4S/\pi)^{1/2}$, where S is the projected colony area. All the dashed lines are best-fit trend lines of the experimental data points.

contractility. We find that the dimples are deeper for softer hydrogels and larger cell colonies [Fig. 2(a)], indicating that the dimple may be a surface effect counteracted by gel elasticity. In addition, when decreasing the fibronectin density coated on the hydrogel surface, the dimple depth decreases [Fig. 2(b)], again suggesting that cell-hydrogel adhesion drives dimpling. We rationalize that a large cell colony has a larger adhesion area and, thus, a large driving force for dimpling, which explains the size dependence. Taken together, these results show that soft hydrogels dimple under both active cell traction and the interfacial stresses, causing morphological changes of the cell colony cultures.

To understand those observations, we examine whether the cell colony indentation into the soft hydrogels can be captured by classical contact mechanics. In the absence of external loads, the JKR theory [30] assumes a negligible elastocapillary effect and predicts a scaling law $E^*d \sim (E^*R)^{1/3}$ for a spherical particle of radius R . Here, E^* is the effective Young's modulus defined by $1/E^* = (1 - \nu_H^2)/E_H + (1 - \nu_C^2)/E_C$, where ν denotes the Poisson's ratio, E denotes the Young's modulus, and the subscripts H and C denote the hydrogel and cell colony, respectively. Considering that both the hydrogel and the cell colony are incompressible, we assume $\nu_H = \nu_C = 0.5$. Taking the radius of the irregular cell colonies $R = (S/\pi)^{1/2}$, where S is the projected area, the classical JKR theory does not fit any of our data at different hydrogel stiffnesses (Fig. S5 [27]), suggesting its limitations in describing the colony-hydrogel contacts.

B. Measurement of interfacial stresses

To explore why the classical JKR theory fails for the cell-ECM contacts, we next employ the NTM [23,31,32] to

measure the interfacial stresses at the colony-hydrogel-medium three-phase interfaces at inhibited cell contractility. The NTM imposes the force balance of the three interfacial stresses at the triple junctions of the three phases [Fig. 3(a)]. By imaging the contact lines and measuring the phase angles, the other two interfacial stresses can be determined provided that one of the interfacial stresses is known. The classical NTM assumes that the bulk stresses of the phases around the contact line are negligible. However, since both the hydrogels and cell colonies are soft, the interfacial stresses may impart non-negligible bulk elastic energies into the soft bodies, which would invalidate the classical Neumann triangle method. However, at a length scale much smaller than the critical capillary length l_S , capillarity becomes dominant over elasticity. Accordingly, as one keeps shrinking the testing volume that encompasses the three-phase contact point, the contribution of the bulk elastic stresses becomes negligible, and the classical Neumann triangle-based balance equation is recovered [23,31,32].

We measure the three interfacial stresses at inhibited cell contractility, denoted by γ_{HM} , γ_{CM} , and γ_{HC} , where the subscripts “H,” “M,” and “C” denote hydrogels, culture medium, and cell colonies, respectively. Since none of the interfacial stresses are known, we first choose an auxiliary system to measure γ_{HM} . This system replaces the cell colonies by 1-octanol (a liquid phase, “o”) on the same hydrogel-medium system, and the associated interfacial stresses are denoted by lowercase subscripts. The interfacial tension between octanol and culture medium (γ_{om}) can be obtained by the pendant drop method. The Neumann triangle of the hydrogel-medium-octanol contacting system is then measured using confocal microscopy [Figs. 3(b) and 3(d), boundary profiles $n = 50$] and used for calculating the

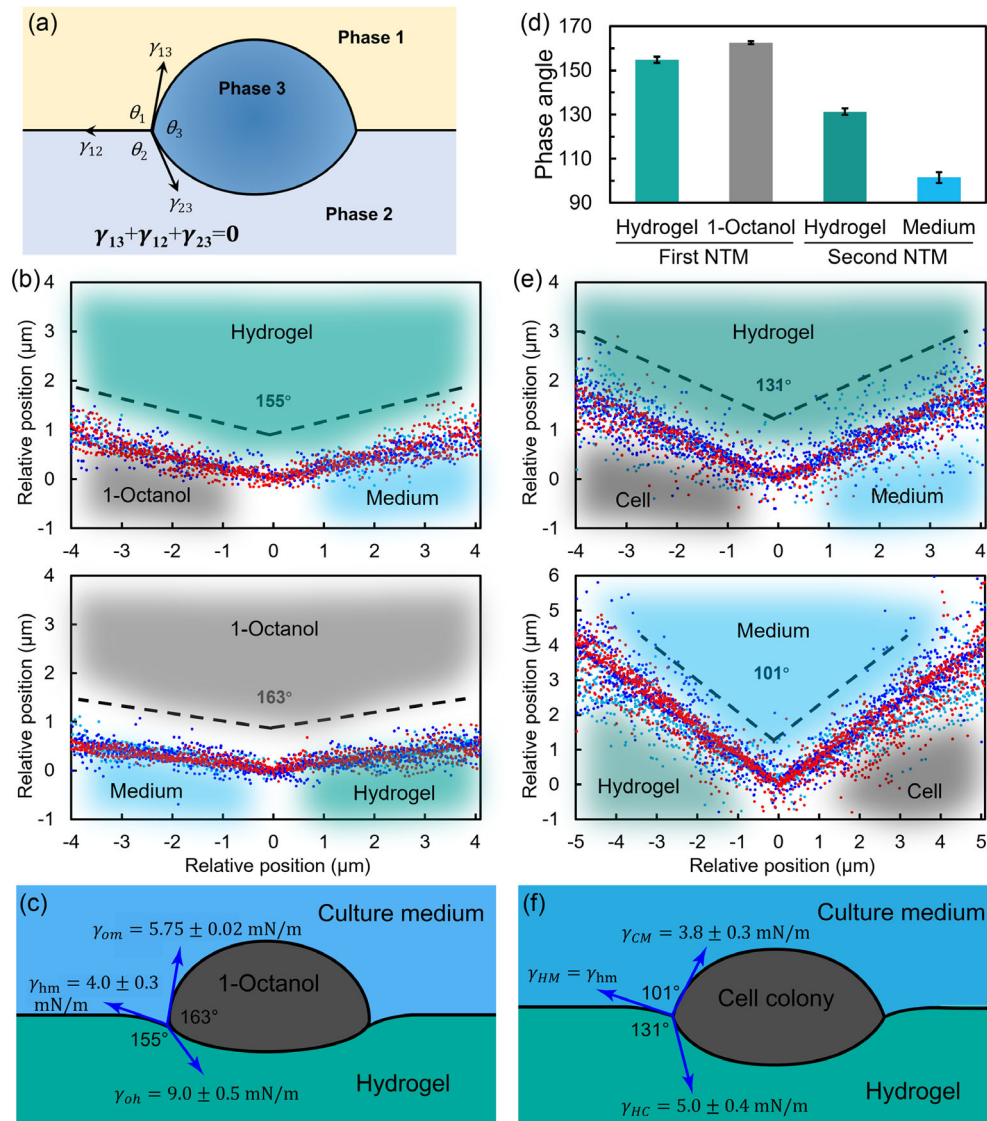


FIG. 3. Measurement of interfacial stresses by NTM. (a) Diagram of the Neumann's triangle. (b) Determination of the hydrogel and 1-octanol phase angles by the plotted phase boundary profiles, in the octanol-medium-hydrogel phase system. For each phase angle, a total of 50 cross-section images from three independent 1-octanol droplets are analyzed. Each chart contains randomly chosen 33 boundary profiles, which are rotated and shifted to align the cusp regions. Each color of the dots resembles the boundary profiles from one droplet. (c) Determination of the interfacial stresses from the phase angles based on the Neumann's triangle scheme. (d) Average phase angles summarized from the plotted phase boundary profiles in the first ($n = 50$) and second ($n = 45$) NTM. Error bars denote standard error of the mean. (e) Determination of the medium and hydrogel phase angles by the plotted phase boundary profiles, in the cell-medium-hydrogel phase system. For each phase angle, a total of 45 cross-section images with three independent cell colonies are analyzed. Each chart contains randomly chosen 33 boundary profiles, which are rotated and shifted to align the cusp regions. Each color of the dots resembles the boundary profiles from one colony. (f) Determination of the interfacial stresses from the phase angles based on the Neumann's triangle.

interfacial tension between hydrogel and culture medium ($\gamma_{hm} = \gamma_{HM}$) [Fig. 3(c)]. Once γ_{HM} is obtained, the Neumann triangle of the hydrogel-medium-colony phases can be measured [Figs. 3(d) and 3(e), boundary profiles $n = 45$], and all the interfacial stresses of the system can be determined by the interfacial force balance equation [Fig. 3(f)].

We estimate the uncertainty of each interfacial tension by the propagation of the uncertainty of γ_{om} and the

uncertainties of measured phase angles. In addition, we confirm that confocal microscopy is adequate to perform the NTM in the capillarity dominant length scale. The measured interfacial stresses are $\gamma_{HM} = 4.0 \pm 0.3$ mN/m, $\gamma_{CM} = 3.8 \pm 0.3$ mN/m, and $\gamma_{HC} = 5.0 \pm 0.4$ mN/m for 0.5 kPa hydrogels. Based on a previous study [33], we estimate the Young's modulus of the HCT-8 colony E_C on the $E_H = 0.5$ kPa hydrogel to be less than 1.4 kPa.

Assuming both the cell colony and the hydrogels are incompressible, the shear modulus G is related to the Young's modulus E by $G = E/3$. Inhibition of the actomyosin activity with blebbistatin further softens the cells [34]. Therefore, the interfacial stress-dominated length scale in our system should be larger than $l_S = [(\min\{\gamma_{CM}, \gamma_{HC}, \gamma_{HM}\})/(\max\{G_H, G_C\})] = (\gamma_{CM}/G_C) = 8.1 \mu\text{m}$. The submicron resolution of the confocal microscopy is sufficient to capture the contact lines below this critical length.

C. Interfacial stresses indent cell colonies

The measured interfacial stresses allow us to quantify the critical elastocapillary length scale in comparison to the cell colony sizes, therefore implicating the relative importance of capillarity and elasticity of the colony-hydrogel contacts. The classical JKR theory is widely used to predict the indentation depth of a rigid spherical particle into an initially flat elastic substrate [35]. The theory is based on an energy balance between the stored elastic energy in the substrate and the adhesion energy at the contact but neglects the work required to stretch the solid surfaces [23–26]. For cells with inhibited cell contractility, the interfacial stresses deform not only the soft hydrogel, but also the cell colony. Here, we extend the classical JKR model to characterize the colony-hydrogel contacts.

The morphology of the HCT-8 cell colonies, even at inhibited cell contractility, depends on the stiffness of the hydrogels. For relatively soft hydrogels (e.g., 0.2 kPa), the colonies tend to form spheroids, as observed in our experiments. For relatively stiff hydrogels (e.g., 2.6 kPa), the cell colonies tend to form a thin-film-like structure [22]. In the following, we develop a theoretical model for the adhesive contact of a spherical cell colony on relatively soft hydrogels and a computational model for a cylindrical cell colony on relatively stiff hydrogels.

For a relatively soft hydrogel with Young's modulus $E_H = 0.2 \text{ kPa}$, we assume that the indentation is a spherical cap with depth d , contact radius a , and radius of curvature R [Fig. 4(a), left]. Note that the critical elastocapillary length is $l_S = (\gamma_{HM}/G_H) = 60 \mu\text{m}$. Since l_S is on the same order of the size of the cell colonies, the interfacial stress is equally important as the elastic restoring force and should not be neglected. The combined elastic energy stored in the hydrogel and the cell colony is $U_e \sim E^* R^{1/2} d^{5/2}$ [32,36]. The adhesion energy at the hydrogel-colony interface is $U_a = -2\pi w R d$, where $w = \gamma_{HM} + \gamma_{CM} - \gamma_{HC}$ is the adhesion energy density. The work required to stretch the hydrogel surface due to the indentation is $U_s = \pi\gamma_{HM} d^2$. We neglect the work done by surface stress γ_{CM} upon area change of the cell colony. The total energy of the system is approximated as

$$U_T = \beta E^* R^{1/2} d^{5/2} + \pi\gamma_{HM} d^2 - 2\pi w R d. \quad (1)$$

Detailed derivation is documented in Supplemental Material [27], Note I. At equilibrium, $[(\partial U_T)/\partial d] = 0$, which yields

$$\frac{5}{2}\beta E^* R^{1/2} d^{3/2} + 2\pi\gamma_{HM} d - 2\pi w R = 0. \quad (2)$$

The constant $\beta = 8/5\sqrt{3}$ is obtained by matching the classical JKR theory which neglects the effect of the interfacial stress. For a given R , the dimple depth d can be solved from Eq. (2), and the contact radius a is obtained using $a = \sqrt{2Rd - d^2}$. Here, we assume that the interfacial stresses change negligibly for different hydrogel stiffness. The prediction of the dimple depth d versus colony size R for the soft hydrogel case ($E_H = 0.2 \text{ kPa}$) is plotted as the solid black curve in Fig. 4(b). In addition, a logarithmic curve fitting shows that the $d \sim R$ slope is very close to 1 (Fig. S5 [27]), indicating the capillary effect is significant. In fact, for such a soft hydrogel and for relatively small cell colonies, the capillary effect is dominant over elasticity, leading to the generalized Young's law [23]: $d = (w/\gamma_{HM})R$. This linear relationship should well describe the experimental data for small cell colonies on the 0.2 kPa hydrogel, i.e., part of the solid black curve. The close match of the y-intercept $y_0 = -0.19$ in the fitted curve in Fig. S5 [27] with the experimentally measured value $\log(w/\gamma_{HM}) = -0.15$ validates both the linear scaling and the NTM for cell colonies.

On the other hand, for the relatively stiff hydrogel ($E_H = 2.6 \text{ kPa}$), the critical elastocapillary length in this case is $l_S = (\gamma_{HM}/G_H) = 4.6 \mu\text{m}$. As $R \gg l_S$, elastic energy is dominant, and Eq. (2) predicts $E^* d = [(\sqrt{3}\pi w)/2]^{2/3} (E^* R)^{1/3}$. However, the classical JKR theory is not appropriate, since it assumes a spherical particle adhering to an elastic substrate. As an analytical solution is inaccessible, we used the finite element method (FEM) to explore the mechanical equilibrium configuration. A more detailed method description can be found in Sec. IV. Here, we adopt the initial colony shape as a short cylinder with a constant colony volume V_C [Fig. 4(a), right], radius R_Y , and height h . The cross section of the hydrogel substrate is approximated by a rectangle with a size much larger than the cell colonies. The bottom hydrogel surface is held fixed in the vertical direction, while the left and right sides of the hydrogel substrate are held fixed in the horizontal direction. Both the colony and hydrogel are modeled as incompressible neo-Hookean solids (see Supplemental Material [27], Note II). The measured interfacial stresses are applied to the corresponding interfaces using our user-defined axisymmetric surface elements [26].

We assume that at inhibited cell contractility the cell-hydrogel system deforms to minimize the free energy. The total energy in the deformation configuration includes the strain energies stored in the colony and hydrogel and

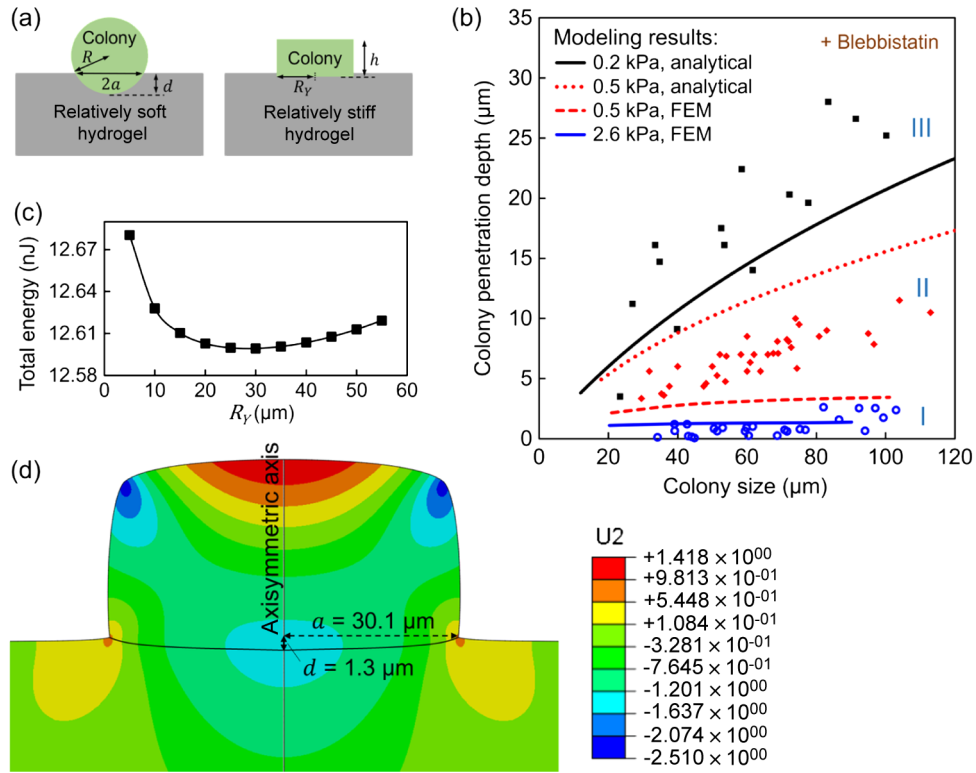


FIG. 4. Modeling of colony indentation driven by interfacial stresses. (a) Schematic of the colony configurations in adhesive contact with a relatively soft hydrogel (left) and a relatively stiff hydrogel (right). For the relatively soft hydrogel, the colony is assumed to be a sphere with a radius R , dimpling depth d , and contact radius a . For the relatively stiff hydrogel, the colony is assumed to be a cylinder with a constant colony volume V_C , where $V_C = \pi R_Y^2 h$ with a variable radius R_Y and a variable height h . (b) Colony dimpling from the modeling results (curves) versus experiments (dots). Colony size is denoted as the equivalent diameter determined by $D = (4S/\pi)^{1/2}$, where S is the colony area. Black, red, and blue dots are 0.2, 0.5, and 2.6 kPa experimental results from Fig. 2(a), respectively, in the presence of blebbistatin. Three regimes are denoted based on the critical elastocapillary length in comparison to the cell colony size. The computational model is suited for regime I and provides the lower bound of regime II. The analytical model is suited for regime III and provides the upper bound of regime II. (c) The total energy, determined by FEM, stored in the system as a function of contact radius R_Y to identify the actual contact radius that minimizes the total system energy. (d) Contour of vertical displacement (U_2) for the deformed colony and hydrogel. The colony volume is fixed as $8.5 \times 10^4 \mu\text{m}^3$, and contact radius is $30.1 \mu\text{m}$ in the reference configuration.

the interfacial energies of all the interfaces. Our simulation strategy is to identify the configuration, at a given colony volume V_C , that minimizes the total energy by varying the radius R_Y . The contact radius a and dimpling depth d can be then extracted from minimum-energy configuration in the simulation. As an example, Fig. 4(c) plots the simulated energy landscape for a fixed $V_C = 8.5 \times 10^4 \mu\text{m}^3$ and varying R_Y from 5 to $55 \mu\text{m}$. It is evident that the total energy reaches its minimum when R_Y is about $30 \mu\text{m}$. Figure 4(d) shows the vertical displacement (U_2) contour for the deformed colony and hydrogel when R_Y is taken to be $30 \mu\text{m}$ in the reference configuration. The corresponding contact radius a and dimpling depth d are found to be 30.1 and $0.3 \mu\text{m}$, respectively. We further predict the indentation depths in colonies with other radii using different colony volumes. The finite element results for the stiff hydrogel case are plotted as the blue curve in Fig. 4(b). The predicted dimple depth of the colonies as a

function of colony size agrees well with the experimental measurements without any fitting parameters.

For intermediate hydrogel stiffness ($E_G = 0.5$ kPa), $l_S = (\gamma_{HM}/G_H) = 24 \mu\text{m}$, both the analytical solution and numerical methods fail to predict the experimental data. The difficulty arises from identifying a rest, reference configuration of the colony-hydrogel systems. However, we find that the analytical solution with the spherically shaped reference configuration gives rise to an upper bound (red dot-dashed line), while the numerical solution with the cylindrically shaped reference configuration of the cell colony to a lower bound (red dashed line), as shown in Fig. 4(b).

D. A two-step traction force microscopy to decouple active traction and interfacial stress

We show that interfacial stresses exist and deform the soft substrate even when the active contraction of the cells

is almost completely inhibited. Such an elastocapillary effect results in a “non-cell-contractile” component of the cell traction forces. As this force has a different origin from the active cell traction force, it is important and necessary to separate them from each other.

Traction force microscopy (TFM) has been developed to measure the extracellular traction sustained by focal adhesions. On the one hand, the active traction force deforms the substrate, generating the stress inside the hydrogel, denoted by σ_H . On the other, the traction force reacts back to the cells, generating cell stress, denoted by σ_C . TFM tracks the displacement of the hydrogel substrate and measures the traction $\mathbf{T} = \hat{\mathbf{n}} \cdot \sigma_H$, where $\hat{\mathbf{n}}$ is the outward normal of the hydrogel. Across the cell-hydrogel interface, a generalized Young-Laplace equation holds:

$$\hat{\mathbf{n}} \cdot (\sigma_H - \sigma_C) = -\kappa\gamma_{\text{HC}}\hat{\mathbf{n}}. \quad (3)$$

In the absence of the interfacial stress ($\gamma_{\text{HC}} \approx 0$), $\hat{\mathbf{n}} \cdot \sigma_C$ is balanced with $\hat{\mathbf{n}} \cdot \sigma_H$, which is regarded as the traction force sustained in the focal adhesions that are transmitted to both the cells and the hydrogel. When capillary force γ_{HC} is non-negligible, the classical TFM measures

$$\mathbf{T} = \hat{\mathbf{n}} \cdot (\sigma_C - \kappa\gamma_{\text{HC}}\mathbf{I}), \quad (4)$$

where \mathbf{I} is the identity tensor. The cellular stress σ_C can be decomposed into two parts; one arises from the active cell contraction, denoted by $\sigma_{C,A}$, and the other from the interfacial forces, denoted by $\sigma_{C,\gamma}$. Note that $\sigma_{C,\gamma}$ and γ_{HC} exist no matter whether cell contractility is inhibited or not. Accordingly, the total traction can be decomposed into an active and passive component: $\mathbf{T} = \mathbf{T}_A + \mathbf{T}_\gamma$. Notably, TFM measures active traction $\mathbf{T} \approx \mathbf{T}_A = \hat{\mathbf{n}} \cdot \sigma_{C,A}$ sustained in the focal adhesions only when the passive cell stress $\sigma_{C,\gamma}$ and the interfacial stress γ_{HC} are both negligible. Otherwise, a passive traction $\mathbf{T}_\gamma = \mathbf{T} - \mathbf{T}_A$ exists:

$$\mathbf{T}_\gamma = \hat{\mathbf{n}} \cdot (\sigma_{C,\gamma} - \kappa\gamma_{\text{HC}}\mathbf{I}). \quad (5)$$

When cell contractility is completely inhibited, active cell stress vanishes: $\sigma_{C,A} = 0$. However, the cell colonies may undergo morphological changes, and TFM at inhibited cell contractility measures

$$\mathbf{T}'_\gamma = \hat{\mathbf{n}}' \cdot (\sigma'_{C,\gamma} - \kappa'\gamma_{\text{HC}}\mathbf{I}) \quad (6)$$

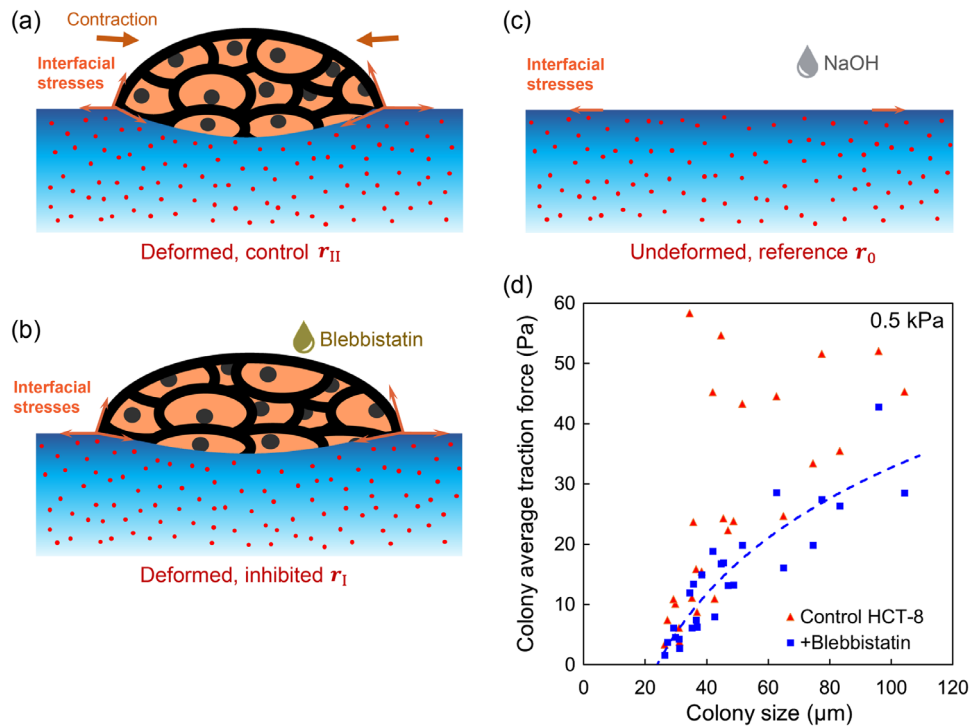


FIG. 5. Separating interfacial stresses from active cell traction. (a)–(c) Schematic description of the two-step TFM, including the configurations of the control condition (a), at inhibited cell contractility (b), and upon detaching cells from the substrate (c). The cell colony (yellow) adheres on the substrate (blue, with embedded red beads). (d) Average traction forces measured by 2D TFM with (blue squares and blue trendline) and without (red triangles) cell contractility inhibition. Colony size is denoted as the equivalent diameter determined by $D = (4S/\pi)^{1/2}$, where S is the colony area. Average traction forces are calculated as the summation of the amplitude of the local traction forces beneath the colony divided by the contact area. Each datum point represents the average traction force from one colony. Each group contains the combined data from at least four parallel experiments. The dashed line is the best-fit trend line for the data points with blebbistatin treatment.

rather than T_γ . If the morphological change is sufficiently small, $T'_\gamma \approx T_\gamma$. In the case that $\sigma_{C,\gamma} \ll \kappa\gamma_{\text{HC}}$, TFM at inhibited cell contractility measures interfacial stresses γ_{HC} .

Based on the above analysis, the active cell traction and interfacial stress can be separated by a two-step TFM, as schematically shown in Figs. 5(a)–5(c). The two-step TFM differentiates the undeformed reference configuration of the hydrogels, the deformed configuration at inhibited cell contractility condition, and the deformed configuration at control condition at which cells are active. For cells cultured on hydrogels, the positions of the fluorescent beads in these configurations can be measured by fluorescence microscopy or by confocal fluorescence microscopy, denoted, respectively, as \mathbf{r}_0 , \mathbf{r}_1 , and \mathbf{r}_{II} . First, \mathbf{r}_{II} can be directly measured, corresponding to the control condition. Second, by adding high-concentration blebbistatin to the culture medium, the deformation due to the active cell traction can be largely excluded, and \mathbf{r}_1 can be measured. Finally, \mathbf{r}_0 in the reference configuration can be captured by detaching the cells from the substrate using sodium hydroxide or detergents. Note that the displacement field $\mathbf{d}_{\text{II}} = \mathbf{r}_{\text{II}} - \mathbf{r}_0$ corresponds to the traction \mathbf{T} and $\mathbf{d}_1 = \mathbf{r}_1 - \mathbf{r}_0$ to the traction \mathbf{T}'_γ ($\approx \mathbf{T}_\gamma$), and the active traction can be approximated by $\mathbf{T}_A \approx \mathbf{T} - \mathbf{T}_\gamma$.

As shown in Fig. 5(d), our 2D TFM shows that the average traction forces of cell colonies, calculated as the summation of the amplitude of the local traction forces beneath the colony divided by the contact area, with inhibited cell contractility is strongly dependent on colony size. For small cell colonies, the total traction is mainly contributed by the interfacial stress. In the absence of the intracellular contractility, 2D TFM can still detect a significant level of “cell traction” [Fig. 5(d), blue squares], comparable to control cells [Fig. 5(d), red triangles], mainly due to the interfacial stresses.

III. CONCLUSIONS

In summary, we have showed that both active cell traction and the interfacial forces can indent cell colonies into hydrogels mimicking soft ECMs. Using the Neumann triangle method, we measured the interfacial stresses at inhibited cell contractility and found that the critical elastocapillary length for such cell-hydrogel contacts is on the same order as the cell colony size, suggesting that the elastocapillary effect is non-negligible in tissue morphogenesis. The elastocapillary effect invalidates the classical JKR contact theory. Theoretical and computational models suitable at different critical elastocapillary length scales are then developed to predict the indentation depths; all agree with the experimental measurements. We further proposed a two-step TFM to separate active cell traction and the interfacial stresses. Given that the capillary forces significantly influence the stress distribution in the cells in the proximity of the interfaces, particularly at

curved surfaces [37], our measurements and models may be further used to correct the conventional monolayer stress microscopy [22,38] in measuring cell stress.

As the elastocapillary effect is non-negligible for single cells and microtissues, capillary force at the cell-ECM contacts may act as a typical mechanical cue, which may trigger both biochemical and mechanical signals and ultimately regulate cell behaviors [22,37]. Noting that active cell traction also acts on the cell-ECM matrix, we may lump all the interfacial forces and define an active elastocapillary length scale. Nevertheless, our study thus represents a step forward to understand capillary force induced mechanotransduction and may open a unique pathway of interfacial engineering to direct and interfere a variety of mechanobiological processes.

IV. METHODS

A. Preparation of cell culture substrates

Polyacrylamide hydrogels with various Young’s moduli (0.20 ± 0.03 kPa, 0.48 ± 0.16 kPa, 2.55 ± 0.17 kPa, $E \pm$ standard deviation) are prepared with the protocol developed previously [39]. Briefly, pre-gel solutions containing varying acrylamide and bis-acrylamide (VWR International) concentrations are degassed under vacuum and are mixed with ammonium persulfate (APS, VWR International) and tetramethylethylenediamine (Millipore-Sigma). A drop of $40 \mu\text{l}$ pre-gel solution is polymerized on a $24 \times 24 \text{ mm}^2$ amino-silanized coverslip. In this way, hydrogel thickness is expected to be more than $60 \mu\text{m}$. To track the cell dimpling and hydrogel deformation, pre-gel solutions are mixed with 1% fluorescent beads ($0.1 \mu\text{m}$ in diameter, Thermo Fisher). To determine the hydrogel boundary in the Neumann’s triangle, pre-gel solutions are mixed with 4% fluorescent beads ($0.04 \mu\text{m}$ in diameter, Thermo Fisher).

Unless otherwise stated, all polyacrylamide hydrogels are functionalized with fibronectin (Millipore-Sigma) by the cross-linker Sulfo-SANPAH (Pierce Chemical) with the protocol developed previously [39]. Briefly, hydrogels are first activated with 0.5 mg/ml Sulfo-SANPAH under 365 nm UV light for 20 min and are subsequently incubated with 0.05 mg/ml fibronectin overnight. For the experiments varying fibronectin coating densities, the total protein concentrations in the final coating solutions remain 0.05 mg/ml , where the fibronectin is replaced by bovine serum albumin (BSA, Thermo Fisher) to decrease the fibronectin coating densities.

Collagen (type I, rat tail, Thermo Fisher) hydrogel substrates are prepared on poly-D-Lysine coated coverslips at a final concentration of 1 mg/ml . Gelation is initiated by neutralizing the collagen solution with $2 \mu\text{l}$ sodium hydroxide (1 M) and $6.6 \mu\text{l}$ $10\times$ DPBS solutions in the cell culture medium for a final volume of $100 \mu\text{l}$. Pre-gel solutions on the coverslips are incubated for 30 min at 37°C . Gels are

washed with cell culture medium thoroughly prior to cell seeding. Fibrin hydrogel substrate on coverslips are prepared by mixing fibrinogen and thrombin (Enzyme Research Laboratories) solutions in the cell culture medium. The final concentrations for fibrinogen and thrombin are 4 mg/ml and 5 U/ml, respectively. The mixture on the coverslips is incubated for 30 min at 37 °C. To inhibit the degradation of collagen and fibrin gels, 6-aminocaproic acid (Millipore-Sigma) at 1 mM and MMP inhibitor I (Millipore-Sigma) at 30 μ M are used during the entire cell culture and imaging periods.

B. Cell cultures and imaging

Human colon carcinoma cells (HCT-8) are cultured in Roswell Park Memorial Institute (RPMI-1640, Millipore-Sigma) supplemented with 10% (v/v) horse serum (ATCC) and 1% (v/v) penicillin-streptomycin (R&D Systems). NIH/3T3 fibroblast cells are cultured in RPMI-1640 (Millipore-Sigma) supplemented with 10% (v/v) fetal bovine serum (FBS, R&D Systems) and 1% (v/v) penicillin-streptomycin. Madin-Darby canine kidney epithelial cells (MDCK) are cultured in modified Eagle's medium (MEM) supplemented with 10% (v/v) FBS and 1% (v/v) penicillin-streptomycin. All cells are incubated at 37 °C in an incubator with 5% CO₂ and 90% humidity. Blebbistatin (Millipore-Sigma), unless otherwise stated, is used at a concentration of 25 μ M overnight to inhibit cell contraction. For inverted cell culture, after cell seeding overnight onto PAA hydrogels polymerized on coverslips, the coverslips are flipped so that the cells are facing down below the hydrogels. Cells under this condition are incubated for 8 h before imaging, and during the imaging period the culture is still inverted.

For 3D imaging, *z*-stacked images are taken with confocal microscopy (Olympus FV1000) with a 40x water-immersion lens (NA = 1.15, *x/y* resolution 0.29 μ m, *z* resolution 0.39 μ m). Images are processed with ImageJ to illustrate the 3D structures. The maximal measurement errors of colony size and dimpling depth can be estimated based on the confocal microscopy resolutions.

C. Staining

To locate the cell boundary, living cells are stained with 8 μ g/ml fluorescein diacetate (FDA, Thermo Fisher) for 5 min. To locate the boundary of cell culture medium in the Neumann's triangle from phases medium-octanol-hydrogel, medium is made fluorescent with 8 μ g/ml FDA incubation for 1 h at 37 °C before imaging.

D. Measurement of interfacial tensions

The interfacial tension between cell culture medium and 1-octanol is measured based on the pendant drop method described previously [40] and is determined to be $\gamma_{om} = 5.75 \pm 0.02$ mN/m (mean \pm SEM, $n = 4$). Other

interfacial tensions are determined by the Neumann's triangle-based contact line method. 3D images around the three-phase mutual contact region are captured to obtain the cross-section images. A cross-section image is selected for further analysis only if the cross section is perpendicular to the three-phase contact line. In a cross-section image, the phase boundaries are linearly fitted by polylines, and the intersection angles are determined based on the slopes of the fitted lines. From the Neumann's triangle, the other interfacial tensions are thus calculated via the law of sines. The uncertainty of each interfacial tension is estimated by the propagation of uncertainties of γ_{om} and measured phase angles.

E. FEM

The finite element model is implemented in the commercial FEM software ABAQUS. The colony and hydrogel are modeled as incompressible neo-Hookean solids. On the boundaries of the axisymmetric axis (left edge) and right edge, no radial displacement or shear traction is allowed; on the bottom edge, the vertical displacement and shear traction are both zero. Hybrid axisymmetric elements CAX4H and CAX3H are used to simulate the incompressibility of the material. Surface finite elements are attached to all the interfaces to model the surface stresses. To balance the accuracy and efficiency of the computation, we choose a fine mesh near the colony, while far away the element size is coarse. Our convergence test shows that further refinement of the mesh does not affect the finite element results. To compute the total energy in the deformed configuration, we obtain the strain energies of the colony and hydrogel directly from ABAQUS and determine the areas of different interfaces (i.e., hydrogel-culture medium, hydrogels-colony, and colony-culture medium interfaces) from the deformed surface profile. The total energy is then given by adding the strain energies stored in the colony and hydrogel to the interfacial energies of all the surfaces (the product of surface energies and corresponding interfacial areas).

F. Traction force microscopy

2D TFM is conducted based on our previous protocol [22]. Briefly, fluorescent bead images are taken by fluorescent microscopy to trace the substrate displacement field. For contractility inhibit experiments, the cells are treated with blebbistatin at 50 μ M for 1 h. To obtain the displacement field, the images are processed with particle image velocimetry. The traction force field is resolved via the Boussinesq solution. In calculating average traction forces, we first calculate the local amplitude of the vectors: $|\mathbf{T}_i|$. The average traction force is then calculated as $(1/A) \sum_i |\mathbf{T}_i| A_i$, where A_i is the area (pixel) on which the local traction force \mathbf{T}_i is applied and A is the projected area of the cell colony.

ACKNOWLEDGMENTS

S. Z. designed the project. X. S. conducted the experiments. X. S., Z. L., L. F., T. Z., and C. H. performed the analytical and FEM analyses. The manuscript was prepared by X. S., Z. L., L. F., and S. Z. S. Z. acknowledges the support of the National Science Foundation (CMMI 1933398); S. Z. and X. S. acknowledge the support of Penn State Convergence Seed Grant Award.

The authors declare no competing interest.

-
- [1] C. Pérez-González, R. Alert, C. Blanch-Mercader, M. Gómez-González, T. Kolodziej, E. Bazellieres, J. Casademunt, and X. Trepat, *Active Wetting of Epithelial Tissues*, *Nat. Phys.* **15**, 79 (2019).
- [2] P. L. Ryan, R. A. Foty, J. Kohn, and M. S. Steinberg, *Tissue Spreading on Implantable Substrates Is a Competitive Outcome of Cell-Cell vs. Cell-Substratum Adhesivity*, *Proc. Natl. Acad. Sci. U.S.A.* **98**, 4323 (2001).
- [3] S. Douezan, K. Guevorkian, R. Naouar, S. Dufour, D. Cuvelier, and F. Brochard-Wyarta, *Spreading Dynamics and Wetting Transition of Cellular Aggregates*, *Proc. Natl. Acad. Sci. U.S.A.* **108**, 7315 (2011).
- [4] T. Razafiarison, U. Silván, D. Meier, and J. G. Snedeker, *Surface-Driven Collagen Self-Assembly Affects Early Osteogenic Stem Cell Signaling*, *Adv. Healthcare Mater.* **5**, 1481 (2016).
- [5] T. Razafiarison, C. N. Holenstein, T. Stauber, M. Jovic, E. Vertudes, M. Loparic, M. Kawecki, L. Bernard, U. Silvan, and J. G. Snedeker, *Biomaterial Surface Energy-Driven Ligand Assembly Strongly Regulates Stem Cell Mechano-sensitivity and Fate on Very Soft Substrates*, *Proc. Natl. Acad. Sci. U.S.A.* **115**, 4631 (2018).
- [6] R. C. Cammarata, *Surface and Interface Stress Effects in Thin Films*, *Prog. Surf. Sci.* **46**, 1 (1994).
- [7] D. Kramer and J. Weissmüller, *A Note on Surface Stress and Surface Tension and Their Interrelation via Shuttleworth's Equation and the Lippmann Equation*, *Surf. Sci.* **601**, 3042 (2007).
- [8] R. A. Foty, C. M. Pflieger, G. Forgacs, and M. S. Steinberg, *Surface Tensions of Embryonic Tissues Predict Their Mutual Envelopment Behavior*, *Development* **122**, 1611 (1996).
- [9] G. S. Davis, H. M. Phillips, and M. S. Steinberg, *Germ-Layer Surface Tensions and "tissue Affinities" in Rana Pipiens Gastrulae: Quantitative Measurements*, *Dev. Biol.* **192**, 630 (1997).
- [10] M. S. Steinberg, *Adhesion in Development: An Historical Overview*, *Dev. Biol.* **180**, 377 (1996).
- [11] C. Huang, Y. Zhang, H. Yuan, H. Gao, and S. Zhang, *Role of Nanoparticle Geometry in Endocytosis: Laying down to Stand up*, *Nano Lett.* **13**, 4546 (2013).
- [12] C. Huang, P. J. Butler, S. Tong, H. S. Muddana, G. Bao, and S. Zhang, *Substrate Stiffness Regulates Cellular Uptake of Nanoparticles*, *Nano Lett.* **13**, 1611 (2013).
- [13] Q. Wei, C. Huang, Y. Zhang, T. Zhao, P. Zhao, P. Butler, and S. Zhang, *Mechanotargeting: Mechanics-Dependent Cellular Uptake of Nanoparticles*, *Adv. Mater.* **30**, 1707464 (2018).
- [14] X. Liu, J. Y. Lim, H. J. Donahue, R. Dhurjati, A. M. Mastro, and E. A. Vogler, *Influence of Substratum Surface Chemistry/Energy and Topography on the Human Fetal Osteoblastic Cell Line HFOB 1.19: Phenotypic and Genotypic Responses Observed in Vitro*, *Biomaterials* **28**, 4535 (2007).
- [15] J. Li, D. Han, and Y. P. Zhao, *Kinetic Behaviour of the Cells Touching Substrate: The Interfacial Stiffness Guides Cell Spreading*, *Sci. Rep.* **4**, 3910 (2014).
- [16] S. R. K. Vedula, G. Peyret, I. Cheddadi, T. Chen, A. Brugués, H. Hirata, H. Lopez-Mendez, Y. Toyama, L. Neves De Almeida, X. Trepat, C. T. Lim, and B. Ladoux, *Mechanics of Epithelial Closure over Non-Adherent Environments*, *Nat. Commun.* **6**, 6111 (2015).
- [17] Q. Wei, X. Shi, T. Zhao, P. Cai, T. Chen, Y. Zhang, C. Huang, J. Yang, X. Chen, and S. Zhang, *Actin-Ring Segment Switching Drives Nonadhesive Gap Closure*, *Proc. Natl. Acad. Sci. U.S.A.* **117**, 33263 (2020).
- [18] E. Theveneau, L. Marchant, S. Kuriyama, M. Gull, B. Moepps, M. Parsons, and R. Mayor, *Collective Chemotaxis Requires Contact-Dependent Cell Polarity*, *Dev. Cell* **19**, 39 (2010).
- [19] B. Sun, J. Lembong, V. Normand, M. Rogers, and H. A. Stone, *Spatial-Temporal Dynamics of Collective Chemotaxis*, *Proc. Natl. Acad. Sci. U.S.A.* **109**, 7753 (2012).
- [20] R. Sunyer, V. Conte, J. Escribano, A. Elosegui-Artola, A. Labernadie, L. Valon, D. Navajas, J. M. García-Aznar, J. J. Muñoz, P. Roca-Cusachs, and X. Trepat, *Collective Cell Durotaxis Emerges from Long-Range Intercellular Force Transmission*, *Science* **353**, 1157 (2016).
- [21] X. Tang, T. B. Kuhlenschmidt, J. Zhou, P. Bell, F. Wang, M. S. Kuhlenschmidt, and T. A. Saif, *Mechanical Force Affects Expression of an in Vitro Metastasis-like Phenotype in HCT-8 Cells*, *Biophys. J.* **99**, 2460 (2010).
- [22] Y. Zhang, X. Shi, T. Zhao, C. Huang, Q. Wei, X. Tang, L. C. Santy, M. T. A. Saif, and S. Zhang, *A Traction Force Threshold Signifies Metastatic Phenotypic Change in Multicellular Epithelia*, *Soft Matter* **15**, 7203 (2019).
- [23] R. W. Style, C. Hyland, R. Boltyskiy, J. S. Wettlaufer, and E. R. Dufresne, *Surface Tension and Contact with Soft Elastic Solids*, *Nat. Commun.* **4**, 2728 (2013).
- [24] Z. Cao, M. J. Stevens, and A. V. Dobrynin, *Adhesion and Wetting of Nanoparticles on Soft Surfaces*, *Macromolecules* **47**, 3203 (2014).
- [25] C.-Y. Hui, T. Liu, T. Salez, E. Raphael, and A. Jagota, *Indentation of a Rigid Sphere into an Elastic Substrate with Surface Tension and Adhesion*, *Proc. R. Soc. A* **471**, 20140727 (2015).
- [26] Z. Liu, K. E. Jensen, Q. Xu, R. W. Style, E. R. Dufresne, A. Jagota, and C. Y. Hui, *Effects of Strain-Dependent Surface Stress on the Adhesive Contact of a Rigid Sphere to a Compliant Substrate*, *Soft Matter* **15**, 2223 (2019).
- [27] See Supplemental Material at <http://link.aps.org/supplemental/10.1103/PhysRevX.12.021053> for Supplemental Figs. S1 to S5 and Supplemental Notes I and II.
- [28] H. M. Zhang, H. H. Ji, T. Ni, R. N. Ma, A. Wang, and X. D. Li, *Characterization of Blebbistatin Inhibition of Smooth Muscle Myosin and Nonmuscle Myosin-2*, *Biochemistry* **56**, 4235 (2017).

- [29] K. A. Beningo, K. Hamao, M. Dembo, Y. li Wang, and H. Hosoya, *Traction Forces of Fibroblasts Are Regulated by the Rho-Dependent Kinase but Not by the Myosin Light Chain Kinase*, *Arch. Biochem. Biophys.* **456**, 224 (2006).
- [30] K. L. Johnson, K. Kendall, and A. D. Roberts, *Surface Energy and the Contact of Elastic Solids*, *Proc. R. Soc. A* **324**, 301 (1971).
- [31] R. W. Style, A. Jagota, C.-Y. Hui, and E. R. Dufresne, *Elastocapillarity: Surface Tension and the Mechanics of Soft Solids*, *Annu. Rev. Condens. Matter Phys.* **8**, 99 (2017).
- [32] R. W. Style, R. Boltyanskiy, Y. Che, J. S. Wettlaufer, L. A. Wilen, and E. R. Dufresne, *Universal Deformation of Soft Substrates near a Contact Line and the Direct Measurement of Solid Surface Stresses*, *Phys. Rev. Lett.* **110**, 066103 (2013).
- [33] X. Tang, Q. Wen, T. B. Kuhlenschmidt, M. S. Kuhlenschmidt, P. A. Janmey, and T. A. Saif, *Attenuation of Cell Mechano-sensitivity in Colon Cancer Cells during In Vitro Metastasis*, *PLoS One* **7**, 1 (2012).
- [34] J. C. Martens and M. Radmacher, *Softening of the Actin Cytoskeleton by Inhibition of Myosin II*, *Pflugers Arch. Eur. J. Physiol.* **456**, 95 (2008).
- [35] K. L. Johnson, *Contact Mechanics* (Cambridge University Press, Cambridge, England, 1985).
- [36] D. Maugis and M. Barquins, *Adhesive Contact of Sectionally Smooth-Ended Punches on Elastic Half-Spaces: Theory and Experiment*, *J. Phys. D* **16**, 1843 (1983).
- [37] T. Zhao, Y. Zhang, Q. Wei, X. Shi, P. Zhao, L. Q. Chen, and S. Zhang, *Active Cell-Matrix Coupling Regulates Cellular Force Landscapes of Cohesive Epithelial Monolayers*, *npj Comput. Mater.* **4**, 10 (2018).
- [38] D. T. Tambe, C. Corey Hardin, T. E. Angelini, K. Rajendran, C. Y. Park, X. Serra-Picamal, E. H. Zhou, M. H. Zaman, J. P. Butler, D. A. Weitz, J. J. Fredberg, and X. Trepap, *Collective Cell Guidance by Cooperative Intercellular Forces*, *Nat. Mater.* **10**, 469 (2011).
- [39] J. R. Tse and A. J. Engler, *Preparation of Hydrogel Substrates with Tunable Mechanical Properties*, *Curr. Protoc. Cell Biol.* **47**, 10 (2010).
- [40] J. Jůza, *The Pendant Drop Method of Surface Tension Measurement: Equation Interpolating the Shape Factor Tables for Several Selected Planes*, *Czech. J. Phys.* **47**, 351 (1997).